

On the complex three-dimensional amplitude point spread function of lenses and microscope objectives: theoretical aspects, simulations and measurements by digital holography

A. MARIAN^{*1}, F. CHARRIÈRE^{*1}, T. COLOMB*,

F. MONTFORT*, J. KÜHN*, P. MARQUET† &

C. DEPEURSINGE*

**Ecole Polytechnique Fédérale de Lausanne (EPFL), Imaging and Applied Optics Institute,
Station 17, CH-1015 Lausanne, Switzerland*

*†Centre de neurosciences psychiatriques, Département de psychiatrie DP-CHUV, Site de Cery,
CH-1008 Prilly-Lausanne, Switzerland*

Key words. Aberrations identification, aberrations quantification, amplitude point spread function, diffraction models, digital holography, phase measurement, phase point spread function.

Summary

The point spread function is widely used to characterize the three-dimensional imaging capabilities of an optical system. Usually, attention is paid only to the intensity point spread function, whereas the phase point spread function is most often neglected because the phase information is not retrieved in noninterferometric imaging systems. However, phase point spread functions are needed to evaluate phase-sensitive imaging systems and we believe that phase data can play an essential role in the full aberrations' characterization. In this paper, standard diffraction models have been used for the computation of the complex amplitude point spread function. In particular, the Debye vectorial model has been used to compute the amplitude point spread function of $\times 63/0.85$ and $\times 100/1.3$ microscope objectives, exemplifying the phase point spread function specific for each polarization component of the electromagnetic field. The effect of aberrations on the phase point spread function is then analyzed for a microscope objective used under nondesigned conditions, by developing the Gibson model (Gibson & Lanni, 1991), modified to compute the three-dimensional amplitude point spread function in amplitude and phase. The results have revealed a novel anomalous phase behaviour in the presence of spherical aberration, providing access to the quantification of the aberrations.

Correspondence to: Florian Charrière. Ing. phys. dipl. EPFL, Imaging and Applied Optics Institute, BM 4.142, Station 17, CH-1015 Lausanne, Switzerland. Tel: +41 21 693 51 82; fax: +41 21 693 37 01; e-mail: florian.charriere@a3.epfl.ch

¹ These authors have contributed equally to this work.

This work mainly proposes a method to measure the complex three-dimensional amplitude point spread function of an optical imaging system. The approach consists in measuring and interpreting the amplitude point spread function by evaluating in amplitude and phase the image of a single emitting point, a 60-nm-diameter tip of a Near Field Scanning Optical Microscopy fibre, with an original digital holographic experimental setup. A single hologram gives access to the transverse amplitude point spread function. The three-dimensional amplitude point spread function is obtained by performing an axial scan of the Near Field Scanning Optical Microscopy fibre. The phase measurements accuracy is equivalent to $\lambda/60$ when the measurement is performed in air. The method capability is demonstrated on an Achroplan $\times 20$ microscope objective with 0.4 numerical aperture. A more complete study on a $\times 100$ microscope objective with 1.3 numerical aperture is also presented, in which measurements performed with our setup are compared with the prediction of an analytical aberrations model.

1. Introduction

1.1. Theory

Among the techniques available nowadays to characterize an optical imaging system, the point spread function (PSF) takes an important place. In the PSF approach, the object is decomposed into infinitesimal point sources and the image is determined as the superposition of the field distribution corresponding to each point-source object. The complex field distribution, corresponding to such a point-source object, is

defined as the amplitude point spread function (APSF) of the system, whose modulus squared gives the intensity or irradiance point spread function (IPSF) and whose phase gives the phase point spread function (PPSF). Usually, attention has been paid mainly on the IPSF, but the relevance of the PPSF has grown with the development of coherent or partially coherent microscopy techniques that allow phase measurements, including standard interferometric techniques (Mach-Zehnder, white-light, Linnick, etc.). In particular, the development of digital holographic microscopy (DHM) necessitates a thorough determination of APSF. Numerous studies have been performed to compensate for the phase aberrations inherent to coherent optical systems, mainly without *a priori* knowledge of either them or further theoretical analysis (see, e.g. Colomb *et al.*, 2006 which present a new aberrations compensation procedure, conjointly with a review of existing techniques). An appropriate understanding of phase aberrations, based on systematic theoretical analysis of the PPSF, may provide innovative aberrations compensation methods, from which the coherent imaging techniques like DMH will take advantage. Hanser *et al.*, and Braat *et al.*, have recently demonstrated the interest of theoretical PPSF, respectively, by characterizing a wide-field fluorescence microscope through its phase-retrieved pupil functions based on intensity measurement (Hanser *et al.*, 2004), and by retrieving the aberration function of high-NA optical systems with the so-called extended Nijboer-Zernike approach (Braat *et al.*, 2003). In their respective measurement of a lens APSF, Walford *et al.* (2002) and Dändliker *et al.* (2004), have shown how phase singularities, characterized by a phase jump of $\pm\pi$ on a closed path around the singularity ($\oint d\varphi = \pm 2\pi$) play a role in aberrations identification. The study of their 3D conformation has been shown to be closely correlated to the presence and type of aberrations.

The theoretical models used in calculation of the PSF of a lens are based on the diffraction theory. Integral expressions have been developed to compute the 3D diffraction pattern resulting from the diffraction of a circular aperture. A comprehensive review has been given by Gibson (Gibson & Lanni, 1989). They include scalar wave models for both on- and off-axis point sources, based on paraxial approximation. Similarly, vectorial models based on the electromagnetic field theory have been developed (Richards & Wolf, 1959), but for all models attention was paid essentially to the intensity distribution and the phase was generally not considered. Linfoot & Wolf (1956) gave a first detailed description of the 3D phase distribution near the focus of an aberration-free lens, by using the Lommel's functions to evaluate the diffraction integral. Based on the scalar diffraction theory, Farnell (1957) calculated the phase in the image region of a microwave lens and verified also his predictions by experimental measurements (Farnell, 1958). A more efficient way to calculate the intensity and phase distributions near the focus was obtained later by the recourse to fast Fourier transform. This may be applied in the Fraunhofer

approximation where the diffraction integral can be viewed as a Fourier transform of the pupil function (Born & Wolf, 1980; Selligson, 1981; Mills & Thompson, 1986).

An optical system can hardly be totally aberration free. Even if primary optical aberrations are well corrected, as in a high quality and expensive microscope objectives (MOs), aberrations can still result from residual misalignment and slight imperfections of the optics. But more often, they are caused by their inappropriate use in nondesigned conditions such as inadequate cover slip thickness, cover slip refractive index or immersion oil refractive index. They can even arise from the specimen under investigation, generally because of focusing media refractive index mismatch. The aberrations theory has been addressed by many authors (see, e.g. Born & Wolf, 1980). The occurrence of aberrations when a MO is used under inappropriate conditions has been analyzed in detail by Gibson (Gibson & Lanni, 1991), who proposed a simple model, based on the scalar diffraction theory and geometrical optics calculations, in order to quantify these aberrations. The same problem, that is, the focusing through dielectric interfaces with different thicknesses and refractive indices, has been treated in a general context by Török (Török & Varga, 1997; Török, 1998), who developed a rigorous model based on the vectorial theory. Recently, Haeberlé combined the Gibson and the Török models and formulated a very accurate and easy-to-use expression for conventional microscopy (Haeberlé, 2003). All these papers predict only the aberrated IPSF and only few works present the PPSF in the presence of primary aberrations (Selligson, 1981; Mills & Thompson, 1986), for low and moderate NA systems.

In coherent microscopy, DHM in particular, a variety of irradiation schemes may be considered: collimated beam (plane wave), as well as focussed beam (spherical wave). We, therefore focus, in the present paper, on the main component of the microscope which is the MO, lead by the idea of obtaining valuable information in amplitude and phase for a later use in aberrations compensation in DHM. Calculation results of both the IPSF and the PPSF are given in the presence of aberrations for high NA MO in some selected cases. A more complete and systematic review of the phase behaviour for each type of aberration has been carried out by Marian (2005).

1.2. APSF measurement techniques

Usually the PSF is measured by acquiring images of small fluorescent beads with diameter under the instrument resolution limit (Gibson & Lanni, 1991). This method was successfully applied, for the measurement of the axial PSF intended to be used in deconvolution and optical sectioning microscopy (Gibson & Lanni, 1991). The main drawback of this experimentally measured PSF is the low signal-to-noise ratio resulting mainly from the shot noise due to the low-intensity signal provided by such small objects. On the other hand, the PSF is measured on a separate setup, under

nondesigned optical conditions of the microscope, which can be quite different from the experimental imaging conditions. In addition to the required presence of small and isolated structure in the sample, the accuracy of the method decreases under deep specimen imaging conditions.

Anyway, all these measurements only take into account the IPSF, neglecting the phase which can play an essential role, for example, in quantifying the aberrations present in the system to completely characterize a lens or a MO. Selligson (1981) proposed already, a method based on a Mach-Zender interferometer, allowing measuring the IPSF and PPSF of lenses subjected to classical aberrations. However, his method requires a point-to-point scan of the focal region and was quite slow at that time, taking up to 20 min for a grid of 32×32 points and, therefore, needing a carefully stabilized measuring system. Schrader (Schrader & Hell, 1996), Juskaitis (Juskaitis & Wilson, 1998) and Walford (Walford *et al.*, 2002) also proposed to record an interference image of a point object, but several images are necessary to reach this goal and a 3D scan of the focal region is also required. Another approach consists of evaluating the complex wavefront at the exit pupil of the MO: Beverage used a Shack-Hartmann wavefront sensor to directly measure the pupil function combined with a Fourier transform calculus to recover its PSF (Beverage *et al.*, 2002) and Török used a Twyman-Green interferometer for measurement and the Debye-Wolf diffraction theory to predict the complex APSF (Török & Fu-Jen, 2002). It is also possible to retrieve the phase from intensity measurements only: Hanser (Hanser *et al.*, 2004) obtained the complex pupil function from defocused IPSF images of subresolution beads with a phase-retrieval algorithm, whereas Braat *et al.* (2003) retrieved the aberration function of high-NA optical systems with the so-called extended Nijboer-Zernike approach. Dändliker *et al.* (2004) measured the APSF of a microlens with a Mach-Zehnder interferometer modified to obtain high spatial accuracy. The microlens is illuminated by a plane wave and moved three-dimensionally in the system to record the 3D APSF, requiring, therefore, no subresolution object.

We propose here an experimental setup, capable to measure the 3D complex APSF of a first-degree optical system, like a simple lens or a complex MO. The method is derived from digital holography, specifically from DHM, where a MO is inserted in the object arm of an off-axis holographic setup (Cuché *et al.*, 1999). The DHM allows to measure the transverse IPSF and PPSF from a single recorded hologram, whereas at least three images are required with a common phase-shifting techniques used, for example, by Selligson (1981) or Dändliker *et al.* (2004). The axial IPSF and PPSF are obtained by performing a fast nanometre step z-scan within a range of tenths of micrometres and acquiring the corresponding stack of holograms at video rate. The originality of the method lies in its capacity to record the full 3D APSF from a rapid 1D z-scan, minimizing, therefore, the noise contribution from external perturbations during the measurements. The scanning rate is

currently limited by the charge coupled device (CCD) frame rate (25 Hz), and could be drastically improved with a faster CCD. The integration time for a single hologram is in the millisecond range with the current 100 mW laser source. To assess accurate estimation of the axial PPSF, the temporal stability of the system during the holograms stack acquisition is monitored thanks to a second holographic setup inserted in the system.

2. Theoretical models for the calculation of the ideal 3D APSF

Different methods can be used to evaluate the diffraction integral and, therefore, to calculate the 3D APSF of a first-order optical system, where the optical system could be a simple lens as well as a MO represented by its equivalent lens. For example, in the scalar Debye theory, based on the Debye approximation (see Gu, 2000), the field in the focal plane $U(P_2)$ is expressed as a superposition of plane waves of different propagation directions \vec{s} within the solid angle Ω subtended by the lens (see Fig. 1):

$$U(P_2) = \frac{i}{\lambda} \int \int_{\Omega} P(P_1) \exp[i\varphi(P_1)] \exp(-ik\vec{s} \cdot \vec{r}_2) d\Omega, \quad (1)$$

where $P(P_1)$ represents the apodization function in the lens plane (Innes & Bloom, 1966; Gu, 2000), \vec{r}_2 gives the position of the observation point in the focal plane, λ is the wavelength and k is the wavenumber defined as $k = 2\pi/\lambda \exp[i\varphi(P_1)]$, corresponding to the phase aberration function in the pupil plane, may be developed in terms of standard polynomials or Zernike polynomials to distinguish the contribution of each aberration type (spherical, coma, astigmatism, etc.). In this equation, as well as in the rest of the paper, the time dependence of the field $\exp(-i\omega t)$ has been implicitly assumed.

The Debye theory combines in this way the geometrical and the wave optics, because all the individual plane waves

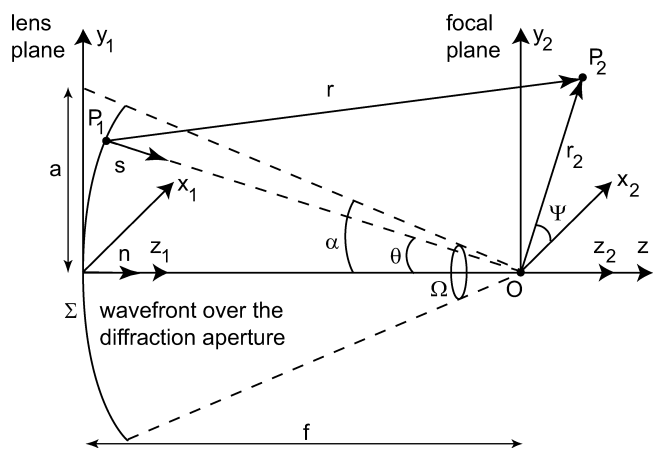


Fig. 1. Scalar Debye theory: focusing of a spherical wave through a lens of focal f , half-aperture a , maximum subtended half angle α .

can be seen as corresponding to the optical rays from the geometrical optics. The Debye integral generally is valid for Fresnel numbers much larger than unity (Wolf & Li, 1981) and in addition, the observation point must be close to the optical axis, especially when aberrations are present in the system (Sheppard, 2000). Within the paraxial limit $\sin \theta \approx \theta$ (Fig. 1), the scalar Debye theory can be consequently simplified, leading to an expression similar to that obtained in the Fresnel approximation (Gu, 2000). A comparison between these two theories (Marian, 2005) shows that significant discrepancies appear if a higher NA is considered (above 0.65). The two models yield comparable results for lower NA, with an easier implementation and a reduced calculation time if the paraxial model is used.

The Debye theory can be generalized in a vectorial form, by taking into account the vectorial nature of the electromagnetic field and the polarization state of the incident field (Ignatowsky, 1919; Richards & Wolf, 1959; Luneburg, 1966). The simulations presented here are based on this theory. The advantage of using the vectorial theory as a first choice is the accuracy in predicting specific features of high NA systems such as apodization and depolarization effects (Gu, 2000), or symmetry break in the focal point (Dorn *et al.*, 2003).

We have considered here the case of an incident field linearly polarized in the x direction, but the expressions could be generalized for any arbitrary polarization state (Mansuripur, 2002). Even if the incident field had a component only along the x direction, the field at the focal plane will have components along all the three directions x (unit vector \vec{i}), y (unit vector \vec{j}) and z (unit vector \vec{k}) (Fig. 2) and for a specific position can be calculated as follows (Gu, 2000):

$$\begin{aligned} \vec{E}(r_2, z_2, \psi) \\ = \frac{\pi i}{\lambda} [i_0 + i_2 \cos(2\psi)] \vec{i} + i_2 \sin(2\psi) \vec{j} + 2ii_1 \cos \psi \vec{k}, \end{aligned} \quad (2)$$

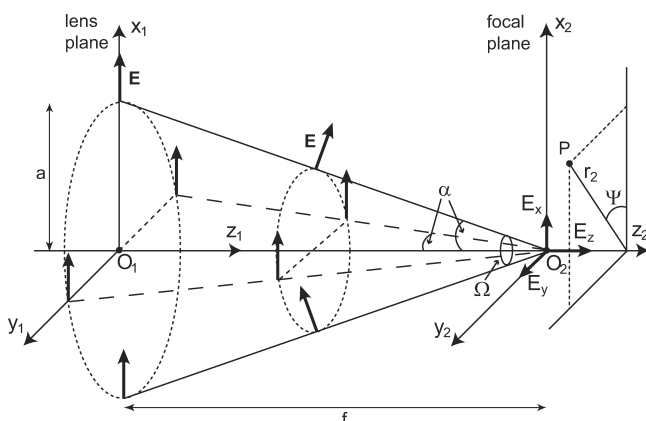


Fig. 2. Vectorial model: focusing of a linearly polarized (x direction) beam through a lens of focal length f , half-aperture a , maximum subtended half-angle α .

where (r_2, z_2) are the radial and axial coordinates of the observation point at the focal plane relative to the focus point and ψ is the azimuth angle defining the radial direction r_2 . When $\psi = 0$, the direction is along the vertical x axis, whereas for $\psi = \pi/2$ the direction is along the horizontal y axis. The definition of this angle is important in the vectorial theory where the symmetry about the optical axis in the focal plane is broken due to the depolarization effect, unlike in the scalar model.

i_0, i_1, i_2 are three integrals expressed as follows:

$$\begin{aligned} i_0 &= \int_0^\alpha P(\theta) \sin \theta (1 + \cos \theta) J_0(kr_2 \sin \theta) \\ &\times \exp(-ikz_2 \cos \theta) d\theta, \\ i_1 &= \int_0^\alpha P(\theta) (\sin \theta)^2 J_1(kr_2 \sin \theta) \\ &\times \exp(-ikz_2 \cos \theta) d\theta, \\ i_2 &= \int_0^\alpha P(\theta) \sin \theta (1 - \cos \theta) J_2(kr_2 \sin \theta) \\ &\times \exp(-ikz_2 \cos \theta) d\theta, \end{aligned} \quad (3)$$

where J_0, J_1, J_2 are the Bessel function of the first kind and of the zero, first and, respectively, second order and the function $P(\theta) = \sqrt{\cos \theta} \exp[i\varphi(\theta)]$ represents the pupil aberration function in which $\sqrt{\cos \theta}$ is the apodization function for a system obeying the Abbe sine condition (Innes & Bloom, 1966; Gu, 2000), like a MO. The Abbe sine condition that is satisfied for all MOs, permits considering, within this vectorial theory, large angles that are not compatible with a paraxial approximation.

The presence of the three components in the image plane:

$$\begin{aligned} E_x &= \frac{\pi i}{\lambda} [i_0 + i_2 \cos(2\psi)], \\ E_y &= \frac{\pi i}{\lambda} i_2 \sin(2\psi), \\ E_z &= \frac{\pi i}{\lambda} 2ii_1 \cos \psi, \end{aligned} \quad (4)$$

leads consequently to three intensity components I_x, I_y, I_z and three phases P_x, P_y, P_z that must be considered as independent.

To illustrate the result of vectorial theory, Fig. 3 presents the intensity and the phase distributions for each component in the focal plane of a $\times 63$ MO with 0.85 NA. The wavelength for the calculations was $\lambda = 532$ nm, and calculations were performed on a $4 \times 4 \mu\text{m}^2$ surface in the xy plane. The structure of each component can be explained by simple geometrical considerations. In our particular case the incident electric vector oscillates along the x direction and, after the refraction by the lens, it is bent in accordance to the refraction law. Consequently, the field at the focus contains not only components with the same polarization as the incident one

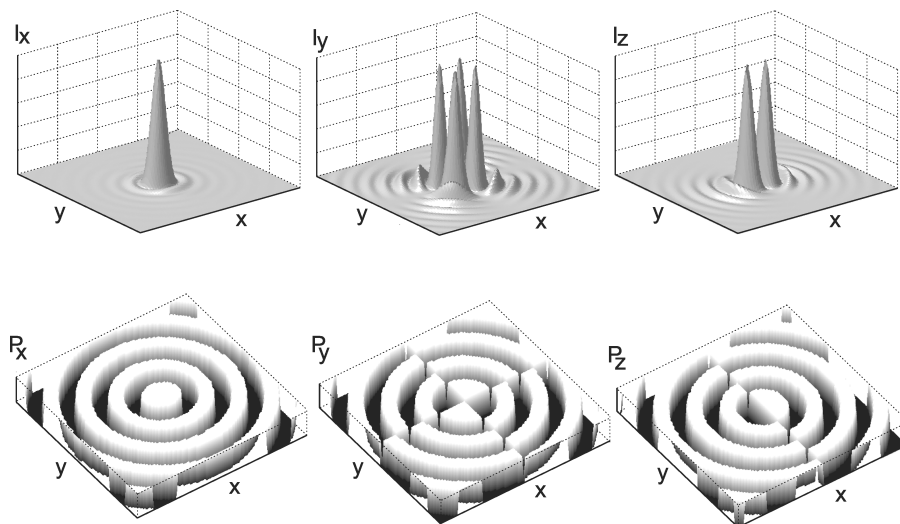


Fig. 3. The x -, y - and z -components of the vectorial transverse APSF (xy) for a $\times 63/0.85$ MO. I_x : I_y : I_z , are in proportion of, respectively, 1: 0.0032: 0.1290. Calculations were performed on a $4 \times 4 \text{ mm}^2$ surface in the xy plane for all the component. The intensity distributions are normalized, the phase distributions are coded between $-\pi$ = black and $+\pi$ = white.

(x direction), but also orthogonal (y direction) and longitudinal (z direction) components. This effect is called depolarization, as the electric vector loses its initial polarization state. In Fig. 2, one can observe that the rays in the yz plane will contribute only to I_x component, the rays in the xz plane will contribute to both the I_x and I_z components, whereas the intermediate rays situated between these planes bring contributions to all the three components I_x , I_y and I_z . The I_x distribution in the xy plane is obtained by superposition of all the x components from each ray and the same reasoning holds for the I_y and I_z distribution. In Fig. 3, the absence of the I_y and I_z in the yz plane is illustrated with the apparition of a zero intensity line along the y direction in the I_y and I_z distributions. Similarly, the absence of the I_y component in the xz plane explains the dark line along the x direction in the I_y distribution.

The total intensity I in the focal plane (the transverse IPSF) can be calculated as the sum of the intensity components

$$\begin{aligned} I &= \vec{E} \vec{E}^* \\ &= (E_x \vec{i} + E_y \vec{j} + E_z \vec{k})(E_x \vec{i} + E_y \vec{j} + E_z \vec{k})^* \\ &= |E_x|^2 + |E_y|^2 + |E_z|^2 \\ &= I_x + I_y + I_z, \end{aligned} \quad (5)$$

but it is undoubtedly improper to define a ‘total phase’, as the phase of the resulting vectorial field \vec{E} , because its orientation is continuously changing. Consequently, the phase of each component P_x , P_y and P_z must be considered apart and calculated as such. Because of the uneven contributions coming from each component, the resulting total intensity in the focal plane does not present a radial symmetry any more but exhibits a radial elliptical distribution. The weights of each component of the total intensity are not equally distributed and for the case of the $\times 63/0.85$ MO considered as typical example,

the maximum intensity components ratio $I_x : I_y : I_z$, taken at the focus, are in proportion of, respectively, 1: 0.0032: 0.1290. These ratios depend on the NA, with increasing weights of I_y and I_z increasing for increasing NA, and observing that the radial elliptical deformation becomes more pronounced as NA increases.

Note that for small NA, the depolarization effect is very small and even disappears, resulting from the fact that for small angles, $J_1(kr_2 \sin \theta)$ and $J_2(kr_2 \sin \theta)$ become negligible compared to $J_0(kr_2 \sin \theta)$. Therefore, the field at the focus (see Eq. 3) can be reasonably approximated by the scalar expression $E(r_2, z_2, \psi) \approx \frac{\pi l}{\lambda} I_0$.

In the case of high NA, I_y is negligible compared to I_x and I_z , and one can observe that the main lobe of the total intensity distribution is essentially broadened because of the depolarization effect observable in the x direction, that is, the direction of polarization, whereas the yz distribution is nearly similar to the yz distribution obtained with the scalar model (Marian, 2005). Therefore, an ellipse can be defined with two orthogonal axes measured by the FWHM (full width at half maximum) of the central lobe of the radial IPSF, along the x direction profile (for $y = 0$) and, respectively, along the y direction profile (for $x = 0$). Then an ellipticity factor can be calculated as the difference in length between the two axes of the ellipse, expressed in percent relatively to the axis length not affected by the depolarization effect (y axis in the case of a x -polarized light). A quantitative comparison shows that for low numerical apertures, this factor is in order of 2.8% for a 0.35 NA ($\approx 20^\circ$ subtended half angle) and, respectively, 6.2% for a 0.5 NA ($\approx 30^\circ$ subtended half angle). The deviation increases significantly with the NA. For an immersion oil $\times 100$ with 1.3 NA MO ($\approx 70^\circ$ subtended half angle), it reaches 30%. We can objectivize the physical limit to the scalar model if

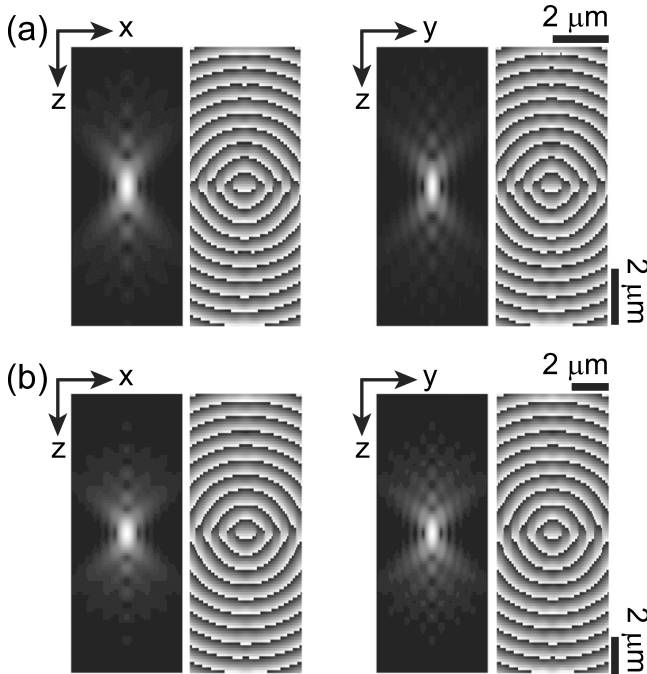


Fig. 4. APSF computed in the axial direction with the vectorial model for a $\times 63/0.85$ MO (a) and a $\times 100/1.3$ MO (b). The intensity distributions are enhanced by a nonlinear distribution of the grey levels, the phase distributions are coded in 8 bits between $-\pi$ = black and $+\pi$ = white.

we consider as tolerable a maximal error corresponding to an ellipticity factor of 10%. This deviation corresponds to a 0.65 NA ($\approx 40^\circ$ subtended half angle), above which the use of the vectorial model is imposed for an accurate APSF description. However, the above considerations are valid for a linear incident polarization only, whereas in the case of an unpolarized beam, an average among all the polarization states occurs and the scalar model can be still used.

Figure 4 presents the axial APSF (total intensity I and phase x component P_x) calculated for a $\times 63/0.85$ MO (Fig. 4a) and, respectively, a $\times 100/1.3$ MO used with a 1.518 immersion oil (Fig. 4b). The simulations were performed using the vectorial theory. We have named axial APSF an axial section along the optical axis through the 3D APSF, whereas the transverse APSF is the xy section at the focal point through the 3D APSF. We present here both the xz and the yz sections. Concerning the phase images, only the P_x component is represented. In the yz plane ($\psi = \pi/2$), because there is only an x -component contribution as already discussed before, only P_x is defined, whereas in the xz plane ($\psi = 0$), both P_x and P_z appear due to the x and z contributions. No y component appears in these planes and, therefore, P_y is not defined. If we consider an intermediate section between xz and yz , for example, for $\psi = \pi/4$, all three phases P_x , P_y , P_z are defined separately. It is in principle possible to measure individually each polarization component in amplitude and phase, for instance by using a dedicated holographic setup (see further) with the appropriate

polarization state in the reference beam interfering with the field emerging from the lens.

3. The 3D APSF in the presence of aberrations

Aberrations are present in most optical imaging systems: lenses, lenses assembly and MO. They are generally a consequence of the fabrication process; spherical aberrations in particular are due to grinding and polishing process of the lens which naturally tends to produce spherical surfaces. These aberrations are usually compensated by the recourse to the assembly of several lenses having complementary geometrical and dielectric characteristics. Other types of aberrations appear when the focused beam crosses one or several dielectric layers, for which the MO has not been designed. To analyze the aberrations appearing when a MO is used under inappropriate conditions, Gibson (Gibson & Lanni, 1991) proposed a simple approach, based on the scalar diffraction theory and geometrical optics calculations. The aberration function is obtained through a calculation involving the ideal design parameters of the MO (cover slip refractive index, cover slip thickness, immersion oil refractive index) and their effective value. The simulations presented here were obtained by implementing the approach suggested by Haeberlé (2003), who combined the Gibson and the vectorial Török models. Figure 5 summarizes the results of the simulations of the APSF of a $\times 100$ MO with 1.3 NA, with nonpolarized light, used under different conditions. If nonpolarized light is diffracted by the MO, the birefringence caused by the high NA MO would mix the cross-polarized components of the beam, while keeping a nonzero correlation among the cross-polarized components of the beam. Therefore, the cross-polarized components of the outgoing beam would cancel out for statistical reason, because the cross-polarized component of the emitted field would be uncorrelated. Therefore, the use of nonpolarized light ensures

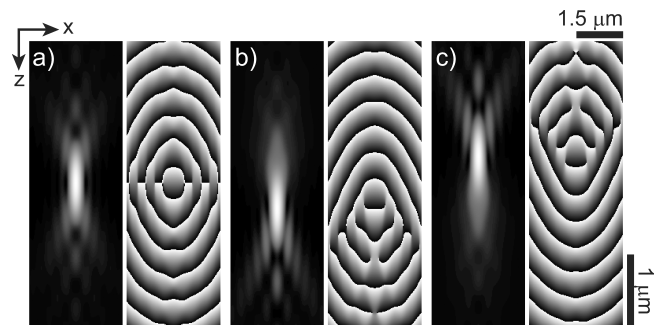


Fig. 5. Axial APSF (xz) examples when the cover slip and the immersion oil refractive index are varied according to Gibson model: ideal case $ng = 1.525$, $ni = 1.518$ (a), cover slip refractive index is varied $ng = 1.530$ (b), immersion oil refractive index is varied $ni = 1.514$ (c). The MO considered here was $\times 100/1.30$. The intensity distributions are enhanced by a nonlinear distribution of the grey levels, the phase distributions are coded in eight bits between $-\pi$ = black and $+\pi$ = white.

the phase map to be identical for all the possible polarization orientations of the reference wave; hence, only one is presented in Fig. 5. The design conditions of the MO are defined by an immersion oil of refractive index equal to 1.518 and a cover slip of 0.17-mm thickness and 1.525 refractive index (standard value for some manufacturers). In this case, the APSF is perfectly symmetric, both transversally and axially (Fig. 5a), as predicted in the case of nonaberrated APSF. Any small deviation from the ideal conditions leads to significant aberrations (Fig. 5b and c). The main lobe of the APSF is shifted from the central position (Fig. 5b and c), which indicates the presence of spherical aberration. It was proved (Gibson, 1991) that high-order spherical aberrations are necessary to describe properly this kind of aberrations. For example, the aberrations induced by the immersion oil refractive index variation can be properly described by using third- and fifth-order spherical aberration, whereas the use of a nondesigned cover slip requires third-, fifth-, seventh- and even more higher-order spherical aberration. It was also observed that the cover slip thickness variation has only a small influence, whereas the cover slip refractive index variation affects drastically the APSF, even for very small variation about 0.001. Figure 5 shows these aberration effects, when the refractive index of the immersion oil was changed from the ideal 1.518 value to 1.514 (Fig. 5b) and when the refractive index of the cover slip was changed from 1.525 to 1.530 (Fig. 5c). For Fig. 5b and c, the corresponding aberration function expressed in term of Zernike coefficients contains mainly the so-called power [$Z_3 = 3^{1/2}(2x^2 + 2y^2 - 1)$] and primary spherical [$Z_{10} = 5^{1/2}(6(x^4 + 2x^2y^2 + y^4 - x^2 - y^2) + 1)$] aberrations, the other coefficients being in those cases negligible. The coefficients values are $Z_3 = 2.36$ and $Z_{10} = -0.56$ for Fig. 5b, respectively, and $Z_3 = -1.96$ and $Z_{10} = -0.48$ for Fig. 5c. The high sensitivity related to the immersion oil refractive index suggests that high attention must be paid at the rapid change of the immersion oil refractive index with the wavelength (about 0.01 throughout the visible spectrum) or due to the temperature variations (about -0.0004 per additional degree). Concerning the cover slip, we must mention also that MOs can be found which include a correction collar to compensate for the cover slip thickness variation. This is done by a slight displacement of some lenses that compose the objective. However, because of the large number of orders of spherical aberration appearing (Gibson, 1991), it is unlikely that the movement of a small number of lenses would be sufficient to compensate for all of the significant orders of the spherical aberration introduced.

As an example of the interest and use of the phase (PPSF) modifications induced by optical aberrations, the following situation has been treated: theoretical calculations of the phase variations along the optical axis have been performed in the presence of aberrations and compared to the absence of aberrations, for the same 100×1.3 NA MO as above. The results are presented in Fig. 6. Indeed, it is usually expected that the phase increases linearly along the optical

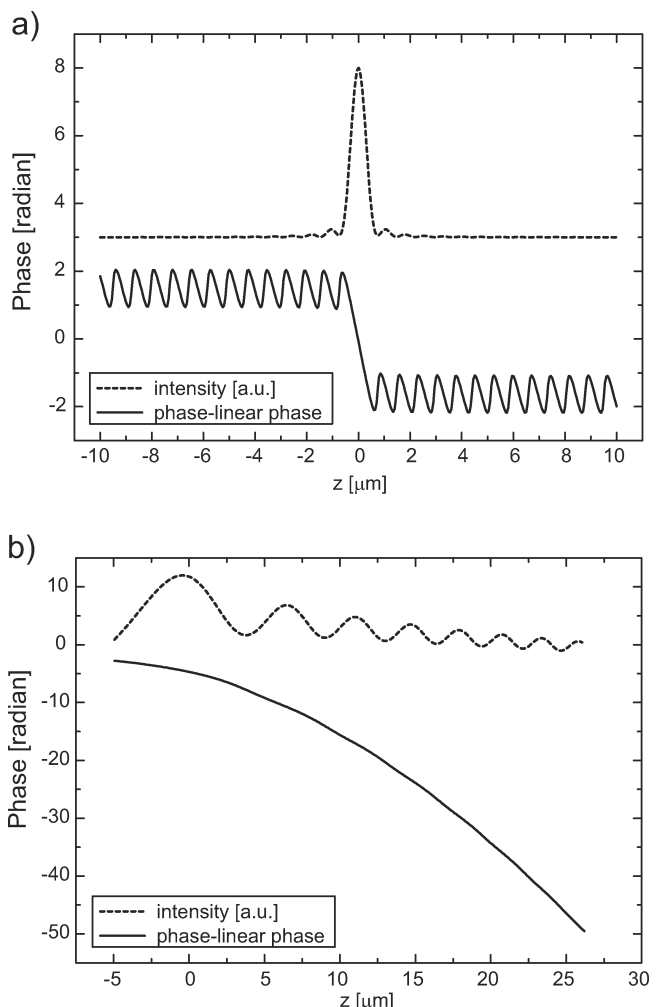


Fig. 6. Axial profiles through the xz section of the IPSF and PPSF for the $\times 100/1.30$ MO, without (a) and with (b) spherical aberrations induced by the use of nondesigned parameters (cover slip, immersion oil). A linear phase corresponding to the displacement along the optical axis has been subtracted in both (a) and (b) to enhance the anomalous phase behaviour in presence of aberration.

axis, proportionally to the displacement, but modulated by the so-called phase anomaly at each passage through an intensity minimum on the optical axis (see, e.g. Farnell, 1958; Born & Wolf, 1980). In the designed conditions, the subtraction of a linear phase from the axial phase leads as expected (Fig. 6a) to the observation of a 2π rapid phase shift for the main axial intensity lobe, and phase jumps smaller than π for all the others secondary lobes. But the phase, except for the modulations described above, remains proportional to the displacement along the optical axis. This is no more the case in the presence of aberrations, where the proportionality is not preserved, as can be seen from Fig. 6b, where is presented a simulation of the axial APSF in the presence of the high-order spherical aberrations induced by the absence of appropriate cover slip and immersion oil. The axial phase, from which the same

linear phase has been subtracted, diverges rapidly from the linear phase when going away from the main intensity lobe. Furthermore, the phase anomalies associated with the passage through the axial intensity minima are weakened and the intensity minima being less deep compared to the designed case, and cannot be distinguished anymore. An experimental verification for this case will be presented further in the paper. These first results suggest that these anomalies in the phase axial phase profile could be exploited to identify the aberrations and possibly to quantify their presence. A more complete and systematic study of the phase nonlinearity, comparable to the ones conducted by Farnell (1958) in the case of microwaves lenses, could be developed and lead to the identification of the aberrations, possibly to quantify their presence from their axial phase profile.

4. APSF measurement

4.1. Experimental setup

Our setup is based on a Mach-Zehnder interferometer configuration. In the object arm, a point-source object is imaged through the MO or through the lens to characterize. (Fig. 7). As a point source we use a near field scanning optical microscopy (NSOM) fibre, with a 60-nm-diameter emitting tip. The light source is a $\lambda = 532$ nm laser (frequency-doubled Nd: YAG) with adjustable power up to 100 mW and the laser is coupled in the optical fibre by a lens. The MO is mounted on micrometric xyz platforms combined with tilt facilities, allowing for proper alignment of the MO to avoid aberrations coming from the setup misalignment. Fine fibre movements, are achieved by a piezoelectric xyz stage, which permits nanometric displacements (1 step = 1.22 nm, within a range of 80 μm). A CCD camera (CCD1) is positioned at a large distance of about 1500 mm to create a sufficiently high magnification (about 1000 \times for a 100 \times MO) image of the point object,

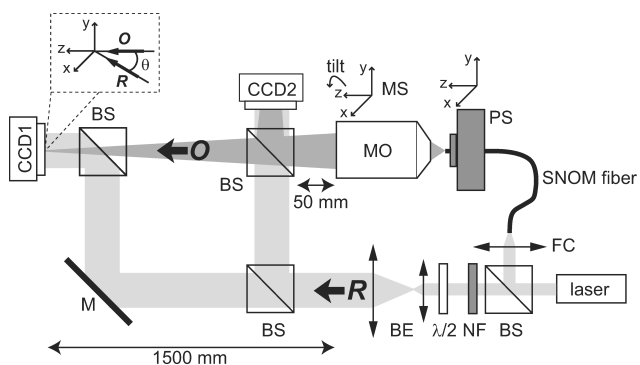


Fig. 7. Experimental setup for the APSF measurement: BS beam-splitter, BE beam expander, NF neutral density filter, $\lambda/2$ half-wave plate, M mirror, FC fibre coupling lens, PS piezo system, MS micrometric stage, MO microscope objective, O object wave, R reference wave. Inset: a detail showing the off-axis geometry at the incidence on the CCD.

in order to obtain an optimal sampling by the CCD sensitive area (512×512 pixels, pixel size 6.7 μm) of the diffraction pattern spatial distribution. As the MOs are now commonly infinity corrected, this large distance also ensures a correct use of the MO, that is, a correct working distance. The setup includes also a second CCD camera (CCD2), which is used for alignments purposes: the MO needs to be carefully aligned on the optical axis defined by the z-scanning direction of the fibre and the position the CCD1 to assure a correct characterization of the MO without external influences coming from the setup misalignments imperfections (tilt, coma, astigmatism). This alignment procedure is revealed to be significantly facilitated when the pupil of the MO is monitored on CCD2. Indeed, due to the large image distance of 1500 mm, a small tilt change of the MO moves the image out of the CCD1. CCD2 is also used to estimate the setup stability during the z-scan, as it will be pointed out further.

The reference wave R is first enlarged by using a beam-expander, and then combined, by means of a beam-splitter, with the object wave O emerging directly from the MO. An off-axis geometry was considered on both CCDs, which means that O and R impinge the hologram plane with different angles (see inset Fig. 7). The angle between O and R must be chosen in order to obtain fringes correctly sampled by the CCD camera. Neutral density filters were used to adjust the light intensity in the reference arm. The adjustment of the intensity ratio between R and O is essential in order to obtain high contrasts images (Charrière *et al.*, 2006). A half-wave plate was also inserted in the setup to control the polarization state in the reference arm, aiming at maximizing the fringes contrast on the hologram. Experimentally, no important change on the hologram fringes contrast is observed when rotating the half-wave plate, attesting for nearly circularly polarized light outgoing of the NSOM tip in the object arm. A remark on the exactness of the method needs to be done: to measure what corresponds to the exact definition of the APSF of the MO, one should in principle scan the image field, that is, moving CCD2, with the NSOM tip remaining fixed in the focus of the MO. Measuring the APSF for a fix image plan and a moving NSOM tip adds little aberration, as the MO is aberration free for only the focus position, but the added aberration remains somehow negligible with regard to the short excursion of the z-scan. Furthermore, moving with an interferometric precision the NSOM tip is easily achieved with the piezoelectric xyz stage; by scanning the image field, the scanning range would be increased by the square of the optical system magnification, reaching centimetres or even metres with a magnification of 1000, making the interferometric measurement extremely difficult if not impossible.

4.2. Holograms reconstruction

In digital holography a CCD camera is used to record the hologram, instead of a photographic plate or photorefractive

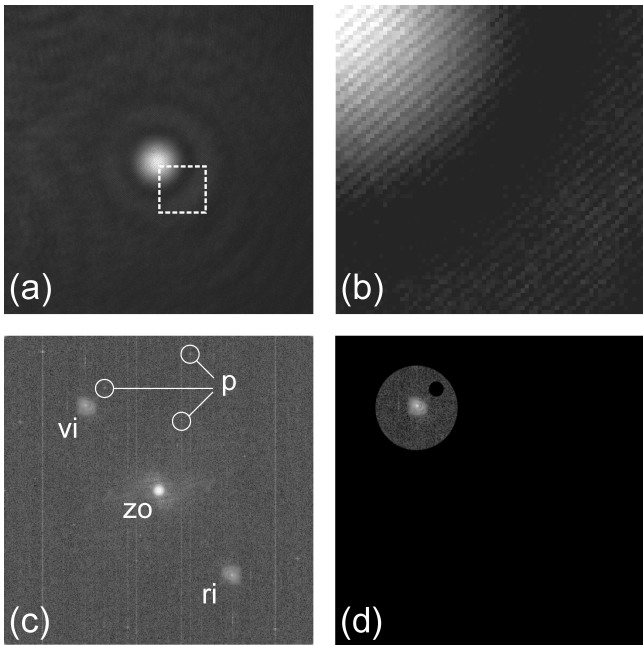


Fig. 8. (a) Example of an experimental 512×512 8-bits hologram; (b) a zoom, corresponding to the dashed square of (a), where the interference fringes appear more visible; (c) the Fourier spectrum of (a) containing the zero order (zo), the real image (ri), the virtual image (vi) and also parasitic interferences spatial frequencies (p); (d) Fourier spectrum after application of the bandpass filter.

crystal traditionally used in classical optical holography. The hologram (Fig. 8a and b) is formed by the interference between the wave field diffracted from the object to be analyzed, that is, the object wave \mathbf{O} and a reference wave \mathbf{R} provided from the same source, in order to keep the coherence properties. The hologram intensity is given by:

$$I_H(x, y) = |\mathbf{R}|^2 + |\mathbf{O}|^2 + \mathbf{R}^* \mathbf{O} + \mathbf{R} \mathbf{O}^*, \quad (6)$$

where \mathbf{R}^* and \mathbf{O}^* denote the complex conjugates of the reference wave and, respectively, the object wave. The digital hologram, resulting from the 2D sampling of $I_H(x, y)$ by the CCD camera, is transmitted to a computer where the hologram reconstruction is numerically performed.

Our reconstruction process consists in evaluating the interferogram using a Fourier-transform method (Malacara & De Vore, 1992) with the following steps. In a first step, we compute the Fourier transform (Fig. 8c) of the hologram. In a second step, only the $\mathbf{R}^* \mathbf{O}$ or the $\mathbf{R} \mathbf{O}^*$ spatial frequencies are selected in the amplitude spectrum, by applying a simple filter (Fig. 8d). Due to the off-axis geometry, these spatial frequencies are separated in the Fourier plane, symmetrically located with respect to the zero-order spatial frequencies. The larger the angle θ between \mathbf{R} and \mathbf{O} is, the better the separation between these spatial frequencies terms will be. In this filter process, we use a filter with a bandwidth as close as possible to the

$\mathbf{R}^* \mathbf{O}$ or $\mathbf{R} \mathbf{O}^*$ bandwidth, in order to keep a maximum of high frequencies and consequently a maximum of details in the reconstructed image. Moreover this filter allows eliminating the influence of parasitic reflections (Fig. 8c) that are not detectable in the hologram due to their low intensity but are clearly visible in the spectrum. The third step simulates the re-illumination of the hologram with the reference wave, considering that in the Fourier space this multiplication by \mathbf{R} corresponds to a translation of the selected frequencies to the centre of the Fourier plane. This procedure must be carefully achieved in order to avoid the introduction of any phase error during the reconstruction. It is performed by an automatic algorithm described in (Colomb *et al.*, 2006). Briefly, this algorithm is based on a calibration on a constant phase surface, which is, in our case, obtained by an important defocus of the NSOM point source: the NSOM point is moved away from the focal point till the object wave recorded on CCD1 corresponds to a cut-off portion of a slowly converging or diverging spherical wave (Wang *et al.*, 1995), where the phase can be assumed to be constant on a transversal plane. Once this calibration of the system is done, the entire stack of holograms is processed in the same way. In a last step, the complex amplitude (i.e. the APSF) is obtained by an inverse Fourier transform and the IPSF and PPSF are afterwards extracted as the modulus squared and the argument of the APSF. The intensity and phase information can be separated in two different images (see, e.g. Fig. 11b), even though only a single hologram is required to restore them. The accuracy in a phase transverse distribution was assessed at about $\lambda/60$ for transmission measurement conducted in air or $\lambda/40$ for oil immersion with a refractive index of 1.518 consistently with the results presented further. We also mention that the values extracted for the PPSF are quantitative values modulus 2π , whereas the IPSF values are extracted up to a multiplicative constant that depends on the intensity of the reference wave.

4.3. Setup stability

The measurement of the axial APSF may require a z-scan of the point object. During this scan, a stack of holograms is obtained by scanning the NSOM tip along the optical axis within a range of tenths of micrometres and with a well-controlled step accuracy of a few nanometres. Each hologram is afterwards reconstructed, following the aforementioned reconstruction process. Consequently, the axial intensity and phase can be estimated. The acquisition of a hologram stack, performed at 25 Hz, takes from seconds to a few minutes, depending on the considered step and range. Therefore, stability must be ensured during the hologram stack acquisition, to provide accurate estimation of the axial PPSF.

As in all interferometric techniques, many factors can affect the phase measurement, principally mechanical vibrations and air turbulences. To overcome these drawbacks, the system was isolated on an antivibratory bench, and the whole stage

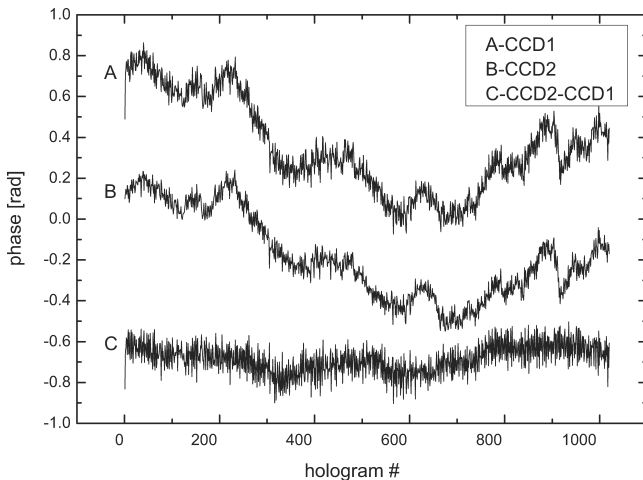


Fig. 9. Temporal phase fluctuations at CCD1, CCD2, and the phase difference between the two phases (1000 holograms recorded in 40 s).

was also protected from air turbulences by curtains. Moreover, the object and the reference arms were also surrounded by plexiglas tubes to minimize the perturbations coming from air turbulences. The particular choice of positioning CCD2 very close to the MO output pupil and the fact of synchronizing it with CCD1 by an external trigger, permit the precise determination and monitoring of the phase fluctuations, which appear along the O and R paths, and along the fibre of the NSOM tip in particular.

A static measure was performed, that is, the NSOM fibre was kept at the same position and a holograms stack was acquired during a time laps equal with the one estimated for an axial z-scan (40 s for 1000 holograms). The holograms recorded by both CCD1 and CCD2 were reconstructed, according to the previously described reconstruction process, and the time fluctuations of the phase were measured and averaged over a small region of about 30×30 pixels. The results are presented in Fig. 9 where it can be noticed that the CCD1 and CCD2 signals are well correlated, with a temporal standard deviation of 0.071 radians (4.11°) calculated onto the difference between the two phase signals. This means that the temporal phase fluctuations observed on the two CCDs are similar, and that no additional noise disturbs the waves along the lengthy path to CCD1.

CCD2, positioned very close to the MO, intercepts the object wave sufficiently far from the focal point (around 1500 mm), so that the wave can be considered as behaving as a cut-off portion of a uniform spherical wave (Wang *et al.*, 1995). Therefore, any displacement of the NSOM fibre along the optical axis is followed by a global and uniform phase change on the wavefront recorded on CCD2, proportional to the displacement of the fibre. When a z-scan is performed, this *a priori* knowledge of the global phase signal to be recorded on CCD2, allows us to evaluate the stability of the setup during the scan.

5. Results and discussions

In order to illustrate the performance of the disclosed method and apparatus, 3D APSF measurements are presented. The example of a special MO will be taken. Some MO types permit the correction of aberration introduced by cover slips of different thickness, by means of an adjustable collar placed on the objective body. By turning the collar to a specific position, corresponding to some particular cover slip thickness, a slight displacement of some built-in lenses inside the MO, introduces variety of aberrations ranging from positive to negative sphericity aberrations, covering therefore, the different possibilities encountered in using cover slips of various thickness. We have used such an objective in order to observe the spherical aberration, which appears when the correction collar is turned from one extremity to the other. The measured MO was a long-distance Achroplan $\times 20$ with a numerical aperture 0.4 and a correction corresponding to a cover slip thickness varying from 0 to 1.5 mm. The MO was mounted in the optical setup without cover slip and the axial APSF has been measured for three particular positions of the correction collar: 0, 0.5 and 1. For each of the three correction collar positions, a stack of 740 holograms was recorded, corresponding to a total axial scan of $44.4 \mu\text{m}$ with 60-nm steps. The holograms were reconstructed and new stacks containing the intensity and respectively the phase images were created, providing the 3D IPSF and respectively the 3D PPSF. The axial APSF is obtained by sectioning the new stacks longitudinally, whereas the transverse APSF is obtained by performing a transversal section at a specific axial position. The results are summarized in Fig. 10.

We can observe that in the 0.5 collar position (Fig. 10b) the APSF is almost aberration free, except maybe a small amount of spherical aberration which can be identified from the slight asymmetry. When the collar is turned symmetrically with respect to the central 0.5 position (Fig. 10a and c), we can observe a symmetrical shift and conjointly, the intensity of the central spot of the IPSF is distributed in the secondary lateral lobes, what is typical for the spherical aberration. Note that for the position 1 of the correction collar (Fig. 10c) the fringes on the holograms were slightly saturated at the maximal intensity position, due to a nonperfect adjustment of the CCD1 dynamic range, what explains the dark spot appearing in the centre of the reconstructed intensity image. The axial shift during the collar turns is clearly observed and the shift distance may be used to quantify the amount of spherical aberration. This example also shows how the proposed method can be used to determine the best correction for given experimental conditions. The insets of Fig. 10b enhance the phase singularities, also called phase vortices or phase dislocations, appearing at the zero intensity points. These singularities are characterized, in a 2D representation, by a phase change of $\pm\pi$ on a closed path around the singularity: $\oint d\varphi = \pm 2\pi$. Great attention has recently been paid

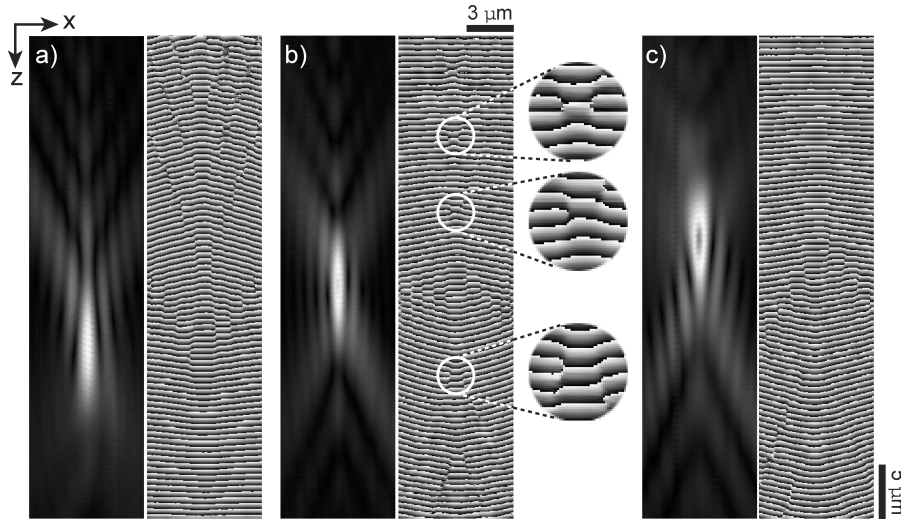


Fig. 10. Axial APSF (amplitude and phase) for different cover slip thickness compensation in an adjustable collar $\times 20$ 0.4 NA microscope objective: collar at position 0 (a), 0.5 (b) and 1 (c). The insets enhance the phase singularities appearing at the zero intensity points. The intensity distributions are enhanced by a nonlinear distribution of the grey levels, the phase distributions are coded in eight bits between $-\pi$ = black and π = white.

to the structure of these zero intensity points both theoretically and experimentally. Totzeck and Tiziani extensively and clearly described this phenomena and its possible use in super-resolution imaging in their study of the 2D complex field diffracted by subwavelength structures (Totzeck & Tiziani, 1997). Walford *et al.* (2002) and Dändliker *et al.* (2004) also discussed these singularities in their measurement of a lens APSF and showed that the study of their 3D conformation can play a role in aberrations identification. Thanks to the shorter acquisition time required for a complete 3D APSF measurement with our system (1D scan vs. 3D scan), the external noise sources including vibrations, air fluctuation or relative movements of the setup components, are minimized, the phase singularities more clearly identifiable in the 2D phase distributions. Furthermore the presented measuring technique is applicable without restriction to high NA MO, as pointed out in the next paragraph.

A more specific study has been conducted on a $\times 100$ MO with 1.3 numerical aperture. The ideal conditions of use for this MO, predicted by the manufacturer, are an immersion oil of 1.518 refractive index and a cover slip of 0.17-mm thickness with 1.525 refractive index. Ideally, the specimen is supposed to be placed immediately behind the cover slip. If the ideal conditions are satisfied, the measured APSF is perfectly axially symmetric, assuming no misalignment in the setup. As it was shown before in the present paper, any small deviation from the ideal parameters induces spherical aberrations and causes significant modifications in the APSF shape. In our measurements, we have chosen to perform the axial scan by moving the object (the NSOM point) instead of the MO. The measurements presented in Fig. 11 (top) were achieved without cover slip but using the ideal immersion oil. The hologram stack was acquired with an axial step of 30.5 nm

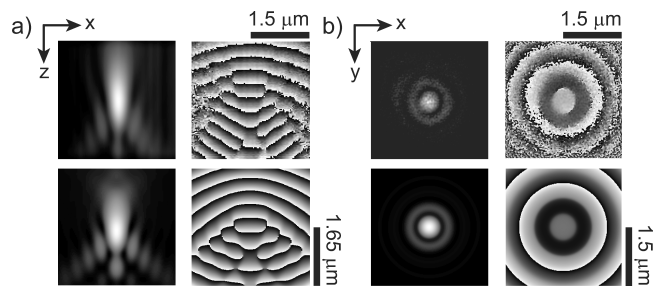


Fig. 11. Axial (a) and radial (b) comparisons in amplitude and phase between experimental APSF measurement (up) and calculated APSF with the Gibson and Lanni model [10] for a $\times 100$ 1.3 NA microscope objective. Measurements performed in oil ($n = 1.518$) without cover slip. The intensity distributions are enhanced by a nonlinear distribution of the grey levels, the phase distributions are coded in 8 bits between $-\pi$ = black and π = white.

and reconstructed by using the process described in subsection 4.2 (4.2 Holograms reconstruction).

Figure 11a compares the measured axial APSF (top) with the theoretically computed axial APSF (bottom). The theoretical simulation was obtained by using the scalar Gibson model (Gibson & Lanni, 1991), adapted for the case when the axial scan is performed by moving the object instead of the MO. Normally the use of a vectorial model, taking into account the polarization of light, is more suitable to calculate the APSF of such a high numerical aperture MO, notably to reproduce the circular asymmetry of the radial APSF. But, in the present work, the scalar model reveals itself sufficient as the light outgoing the NSOM fibre tip is nearly circularly polarized and the measurement is performed on the image side with a small NA. Therefore, the scalar model can be used in first approximation (the xy -distribution prediction will be

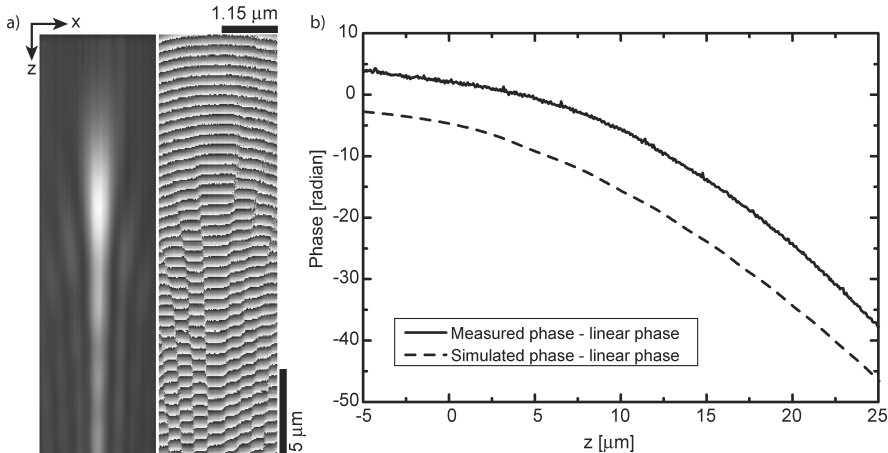


Fig. 12. (a) Measured xz sections of the IPSF and PPSF for the $\times 100/1.30$ MO used under nondesigned conditions (no cover slip, no immersion oil); (b) simulated and measured phase profile behaviour — from which a linear phase corresponding to the displacement along the optical axis has been subtracted — along the optical axis.

somehow too narrow), and one can benefit from its speed advantages for calculations. The z -step in the simulation was 10 nm, which allows explaining the theoretical smoother phase image. The intensity was normalized and the grey levels were distributed nonlinearly to enhance low-intensity details. The phase was wrapped, taking values between 0 and 2π radians. As expected, the axial APSF is asymmetric, due to spherical aberrations caused by the absence of cover slip.

The transverse APSF, obtained by transverse sectioning of the 3D APSF in the plane corresponding to the axial IPSF maximum value, is shown in Fig. 11b: measurement (top) and theoretical simulation (bottom). The airy pattern is clearly visible both in the amplitude and phase images, with its central disk and the surrounding rings. As expected, phase π -jumps are observed at each passage through the amplitude minima. Due to the presence of spherical aberration, the phase is not constant but decreases smoothly toward the centre inside the regions delimited by the airy rings. As one can see from Fig. 11, the analytical model and the measured data are in excellent agreement, assessing the prediction of the Gibson and Lanni approach for calculating the aberrations due to a nondesigned use of the MO.

The last result presented concerns the experimental verification of the novel phase behaviour in the presence of optical aberrations induced by nondesigned conditions of use presented in subsection 3 (3. The 3D APSF in the presence of aberrations). Theoretical calculations and experimental results are presented in Fig. 12, for the same 100×1.3 NA MO as above, used without immersion oil and without cover slip. The broadening of the APSF along the optical axis may be observed in Fig. 12a. As expected, the axial phase, from which a linear phase has been subtracted, diverges rapidly when going away from the main intensity lobe. In can be seen in Fig. 12b that simulation and experiment are in good agreement.

6. Conclusion

We have reviewed in the present paper different models, corresponding to various simplifying assumptions: scalar, paraxial and vectorial. Depending on the NA of MO and polarization of the beam, they can be applied to compute the 3D APSF of a lens or MO. It is obvious that the more adequate model is the vectorial one, including considerations about the polarization state and separate calculus of each field component. The differences between the vectorial and the scalar model are not very significant when low and moderate NA systems are considered, but may become important for high NA systems typically above 0.65 NA. The advantage brought by the scalar model is its simple implementation and reduced computation time, which, for low and moderate NA system can be further reduced by considering the paraxial approximation. For the first time, the complex APSFs are calculated in amplitude and phase according to the vectorial formulation applied to the Gibson model. First calculations reveal the 3D phase distribution within the PSF as a function of polarization, whereas the second ones illustrate the changes accompanying high NA MO under nondesigned conditions. The simulations, performed with the Gibson model, enlighten the phase variation on the optical axis, in the presence of aberrations caused by nondesigned conditions (refractive index, cover slip type): the axial phase is no more simply proportional to the displacement along the axis. This observation, experimentally verified, suggests that the study of the phase variations on the axis could provide a very sensitive indicator of the presence of aberrations, and also as a quantitative measure of the aberrations weight.

Theoretical analyses of imaging systems PSF have been widely and systematically conducted. Nowadays each microscope user can benefit from a better skill in the design of

MOs. Most recent deconvolution algorithms have contributed to the enhancement of the image quality. In this context, the PPSF role, obvious in all phase-sensitive imaging techniques, can also play an essential role in aberrations identifications and quantifications in microscopy as it already has been discussed. The results presented in this paper provide a new contribution to the problem of aberrations identification and removal by introducing the concept of PPSF as a sensitive index to lenses or MO imperfections.

To fulfil experimental requirements we have developed a fast, reliable and quantitative method for measuring the APSF of an optical system, and MOs in particular. A 1D scan, performed by moving a NSOM fibre tip along the optical axis in the focal region of the MO, leads to the full complex 3D description of the APSF after numerically processing the holographic digitally recorded data. The accuracy of the phase determination reaches up to $\lambda/60$ when performed in air. The setup can easily be adapted to the working parameters of a given MO (immersion oil thickness and refractive index, cover slip thickness and refractive index, specimen position, etc.) allowing a precise and reliable characterization of the MO in its using conditions. This effective measurement can be used as a simple and efficient technique to assess the predictions of an analytical model, like the Gibson & Lanni approach used in this paper (Gibson & Lanni, 1991). Furthermore, the knowledge of the exact APSF, giving a direct access to the optical aberrations present in the system, allows, within the frame work of phase-sensitive imaging techniques, including DHM, a precise interpretation of the measured phase on a given specimen by numerically compensating for all these aberrations.

Acknowledgements

This research has been supported by the Swiss National Science Foundation (SNSF) grant 205320-103885/1. The authors gratefully acknowledge Prof. C. J. R. Sheppard for the valuable discussions on theoretical aspects about the PSF. The authors also warmly thank Etienne Cuche, from the start-up company Lyncée Tec SA (www.lynceetec.com), for his enthusiasm and his precious comments on digital holography.

References

- Beverage, J.L., Shack, R.V. & Descour, M.R. (2002) Measurement of the three-dimensional microscope point spread function using a Shack-Hartmann wavefront sensor. *J. Microsc.* **205**, 61–75.
- Born, M. & Wolf, E. (1980) *Principles of Optics*. Pergamon, Oxford.
- Braat, J.M. (2003) Extended Nijboer-Zernike representation of the vector field in the focal region of an aberrated high-aperture optical system. *J. Opt. Soc. Am. A* **22**, 2281–2292.
- Charrière, F., Colomb, T., Montfort, F., Cuche, E., Marquet, P. & Depeursinge, C. (2006) Shot noise influence in reconstructed phase image SNR in digital holographic microscopy. *Appl. Opt.* **45**, 7667–7673.
- Colomb, T., Cuche, E., Charrière, F., Kühn, K., Aspert, N., Montfort, F., Marquet, P. & Depeursinge, C. (2006) Automatic procedure for aberration compensation in digital holographic microscopy and applications to specimen shape compensation. *Appl. Opt.* **45**, 851–863.
- Cuche, E., Bevilacqua, F. & Depeursinge, C. (1999) Digital holography for quantitative and phase-contrast imaging. *Opt. Lett.* **24**, 291–293.
- Dändliker, R., Tortora, P., Vaccaro, L. & Nesci, A. (2004) Measuring optical phase singularities at subwavelength resolution. *J. Opt. A* **6**, 189–196.
- Dorn, R., Quabis, S. & Leuchs, G. (2003) The focus of light — linear polarization breaks the rotational symmetry of the focal spot. *J. Mod. Opt.* **12**, 1917–1926.
- Farnell, G.F. (1957) Calculated intensity and phase distribution in the image space of a microwave lens. *Can. J. Phys.* **35**, 777–783.
- Farnell, G.F. (1958) On the axial phase anomaly for microwave lenses. *J. Opt. Soc. Am. A* **48**, 643–647.
- Gibson, S.F. & Lanni, F. (1989) Diffraction by a circular aperture as a model for three-dimensional optical microscopy. *J. Opt. Soc. Am. A* **6**, 1357–1367.
- Gibson, S.F. & Lanni, F. (1991) Experimental test of an analytical model of aberration in an oil-immersion objective lens used in three-dimensional light microscopy. *J. Opt. Soc. Am. A* **8**, 1601–1613.
- Gu, M. (2000) *Advanced Optical Imaging Theory*. Springer Verlag, Berlin Heidelberg.
- Haeberlé, O. (2003) Focusing of light through a stratified medium: a practical approach for computing microscope point spread functions. Part I: Conventional microscopy. *Opt. Commun.* **216**, 55–63.
- Hanser, B.M., Gustafsson, M.G.L., Agard, D.A. & Sedat, J.W. (2004) Phase-retrieved pupil functions in wide-field fluorescence microscopy. *J. Microsc.* **216**, 32–48.
- Ignatowsky, V.S. (1919) Diffraction by a lens of arbitrary aperture. *Trans. Opt. Inst. Petr.* **4**, 1–36.
- Innes, D.J. & Bloom, A.L. (1966) Design of optical systems for use with laser beams. *Spectra-Phys. Laser Tech. Bull.* **5**, 1–10.
- Juskaitis, R. & Wilson, T. (1998) The measurement of the amplitude point spread function of microscope objective lenses. *J. Microsc.* **189**, 8–11.
- Linfoot, B.E. & Wolf, E. (1956) Phase distribution near focus in an aberration-free diffraction image. *Proc. Phys. Royal Soc. B*, **LXIX**, 823–832.
- Luneburg, R.K. (1966) *Mathematical Theory of Optics*. University of California Press, Berkeley and Los Angeles.
- Malacara, D. & De Vore, S.L. (1992) Interferogram evaluation and wavefront techniques. *Optical Shop Testing* (ed. by D. Malacara). Wiley, New York.
- Mansuripur, M. (2002) *Classical Optics and its Applications*. Cambridge University Press, Cambridge.
- Marian, A. (2005, first published in 2006) *Measurement and interpretation of the 3D amplitude point spread function of lenses and microscope objectives*. PhD thesis, EPFL, Lausanne.
- Mills, J.P. & Thompson, B.J. (1986) Effect of aberrations and apodization on the performance of coherent optical systems. I. The amplitude impulse response. *J. Opt. Soc. Am. A* **3**, 694–703.
- Richards, B. & Wolf, E. (1959) Electromagnetic diffraction in optical systems II. Structure of the image field in an aplanatic system. *Proc. Royal Soc. A* **253**, 358–379.
- Schrader, M. & Hell, S.W. (1996) Wavefronts in the focus of a light microscope. *J. Microsc.* **184**, 143–148.
- Selligson, J.L. (1981) *Phase measurement in the focal region of an aberrated lens*. PhD thesis, University of Rochester, New York.

- Sheppard, C.J.R. (2000) Validity of the Debye approximation. *Opt. Lett.* **25**, 1660–1662.
- Török, P. & Fu-Jen, K. (2002) Point-spread function reconstruction in high aperture lenses focusing ultra-short laser pulses. *Opt. Comm.* **213**, 97–102.
- Török, P. & Varga, P. (1997) Electromagnetic diffraction of light focused through a stratified medium. *Appl. Opt.* **36**, 2305–2312.
- Török, P. (1998) Focusing of electromagnetic waves through a dielectric interface by lenses of finite Fresnel number. *J. Opt. Soc. Am. A* **15**, 3009–3015.
- Totzeck, M. & Tiziani, H.J. (1997) Phase-singularities in 2D diffraction fields and interference microscopy. *Opt. Comm.* **138**, 365–382.
- Walford, J.N., Nugent, K.A., Roberts, A. & Scholten, R.E. (2002) High-resolution phase imaging of phase singularities in the focal region of a lens. *Opt. Lett.* **27**, 345–347.
- Wang, W., Friberg, A.T. & Wolf, E. (1995) Structure of focused fields in systems with large Fresnel numbers. *J. Opt. Soc. Am. A* **12**, 1947–1953.
- Wolf, E. & Li, Y. (1981) Conditions for the validity of the Debye integral representations of focused fields. *Opt. Commun.* **39**, 205–210.